CERN-FASER-CONF-2024-001
April 6, 2024

Search for Axion-Like Particles in Photonic Final States with the FASER Detector at the LHC

FASER Collaboration

The first FASER search for a light, long-lived particle decaying into a pair of photons is reported. The search uses the collected 2022 and 2023 LHC proton-proton collision data at $\sqrt{s} = 13.6$ TeV, corresponding to an integrated luminosity of 57.7 fb^{-1}. A model with axion-like particles (ALPs) dominantly coupling to weak gauge bosons is targeted, probing a mass range between 50 and 500 MeV and couplings to the Standard Model particles, g_{aWW}, between 10^{-5} and 10^{-3} GeV^{-1}. Signal events are characterised by high energy deposits in the electromagnetic calorimeter and no signal in the veto scintillators. One event is observed, compared to a background expectation of 0.42 ± 0.38 events, which is entirely dominated by neutrino interactions. World-leading constraints on ALPs are obtained for masses up to 300 MeV and couplings around 10^{-4} GeV^{-1}, testing a previously unexplored region of parameter space.

CONTENTS

I. INTRODUCTION

The ForwArd Search ExpeRiment (FASER) [1–3] is an experiment at the CERN Large Hadron Collider (LHC) designed to search for light, weakly-interacting particles produced at the ATLAS interaction point (IP1). These particles include the neutrinos and muons of the Standard Model (SM) and also new particles associated with beyond-the-SM (BSM) phenomena.

The FASER detector [4] is positioned on the beam collision axis or line of sight (LOS), 480 m from IP1, offering a relatively large acceptance and efficiency for long-lived particle decays. The detector is in an ideal location to study particles that are produced in proton-proton collisions and so weakly interacting that they can travel through a hundred meters of concrete and rock. The only SM particles reaching the detector through the rock and not deflected by LHC magnets are neutrinos and muons. Neutrinos from colliders were first directly observed using the electronic components of FASER in 2022 data [5]. Neutrinos can also be detected through their interactions with the neutrino-specific passive detector component, FASERν [6], which has been used to discover the first electron neutrinos at colliders [7] and also measure neutrino cross sections in the previously unprobed TeV energy range [8].

Particles in the SM fail to explain dark matter (DM), which highly motivates searches for new particles. These models often involve particles in a hidden sector, weakly interacting with the SM. Depending on their mass and coupling, these particles can be long-lived and potentially decay in FASER. FASER's reach for BSM long-lived particles has been studied in Ref. [9]. The first search for dark photons has been published using the 2022 Run 3 dataset [10] and exploits the signature of a very high-energy electron-positron pair appearing within the detector.

In this note, a search for a light, neutral particle decaying to a pair of photons is reported, and models with axion-like particles (ALPs) are targeted. ALPs are a general class of pseudoscalar particles that includes axions, which are well-motivated by attempts to resolve the strong CP problem [11–13]. The search uses proton-proton collision data collected by FASER in 2022 and 2023 at $\sqrt{s} = 13.6$ TeV, corresponding to an integrated luminosity of 57.7 fb^{-1}. Events are required to have a high energy deposit in the electromagnetic (EM) calorimeter of the FASER detector, as the signature of energetic photon pairs arising from the decay of an ALP, in addition to no upstream activity. Incoming charged particles are vetoed through FASER's scintillator system.

The note is structured as follows: Section II reports the details of the targeted ALP model. The FASER detector is briefly presented in Section III. Section IV summarises the event reconstruction and details about the data and simulation samples used. Sections V–VII describe the core of the analysis, from event selection, to the estimate of the backgrounds and the evaluation of systematic uncertainties. Section VIII reports the results and their statistical interpretation as constraints on the ALP model parameter space. The Appendix contains additional details of the analysis, comparisons to existing bounds, and an event display.

II. AXION-LIKE PARTICLES IN FASER

FASER can probe several types of ALP models [9] and is particularly sensitive to scenarios in which the ALP couples to the SU(2)$_L$ gauge bosons. In this model, the coupling to SU(2)$_L$ gauge bosons is present before electroweak symmetry breaking (EWSB) [14–16]. After EWSB, the ALP couples to both photons and the weak gauge bosons. The phenomenology of the model is determined by the ALP mass and coupling. The corresponding Lagrangian for the ALP a is [14–16]

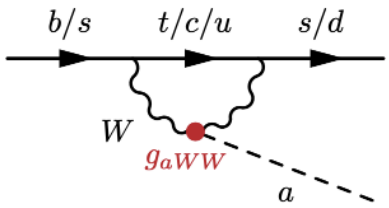

FIG. 1. An example of a quark-level Feynman diagram in which an ALP with W couplings is produced in the FCNC decay of a b- or s-flavoured hadron.

$$\mathcal{L} \supset -\frac{1}{2}m_a^2 a^2 - \frac{1}{4}g_{aWW} a W^{a,\mu\nu}\tilde{W}^a_{\mu\nu} \ , \tag{1}$$

where m_a is the ALP mass, g_{aWW} is the ALP coupling parameter, and $W^{\mu\nu}$ is the SU(2)$_L$ field strength tensor. This model can be viewed as a UV completion of the Physics Beyond Colliders [17] benchmark model BC9, where only couplings to photons were considered.

In the models considered in this study, ALPs arise in decays of b- or s-flavoured hadrons produced at IP1, primarily via flavour-changing neutral current (FCNC) decays. The underlying quark-level Feynman diagram is shown in Figure 1. The dominant production processes, at almost equal rates, include the decays of B^0 and $B^\pm$ mesons into ALPs and various possible strange hadrons. Decays of other B-hadrons, such as B_s mesons, are expected to contribute significantly less to the ALP production rate. In the low m_a range, where kinematically allowed, kaons can also decay into a pion and an ALP. Once produced, the dominant ALP decay mode is into two photons. The decay $a \to \gamma ee$ through an off-shell photon has a branching fraction at the percent level and is negligible for this study.

Figure 2 shows the expected acceptance, efficiency, and signal yield for the ALP model considered in this note as functions of m_a and g_{aWW}. Predictions are obtained using Monte Carlo (MC) samples generated with the `FORESEE` [18] package prior to the detector response simulation (referred to as truth level) and assuming an integrated luminosity of 57.7 fb^{-1}.

Light particles created in B-meson decays are highly collimated around the LOS, leading to a small spread and good acceptance within the FASER detector volume [9]. In the parameter space of interest, typical signal acceptances in the FASER detector volume are of the order of 10^{-6} to 10^{-7} (Figure 2, top left). Given that FASER covers around 10^{-8} of the solid angle of the ATLAS IP and the decay-in-volume probability is $< 0.3\%$, this highlights the beneficial location of FASER for BSM searches.

Since the forward hadron inherits a sizable fraction of the beam energy, the ALPs reaching FASER can have multi-TeV momenta [9]. The efficiency for selecting ALPs with energy above 1.5 TeV (Figure 2, top right) is well above 50% for high coupling values, and is 10% or more for a large part of the parameter space, for example, around ALP masses of 100 MeV and down to couplings of 10^{-5} GeV^{-1}.

Assuming a background-free analysis and a luminosity of 57.7 fb^{-1}, signal yields evaluated at truth level as a function of m_a and coupling g_{aWW} are shown in Figure 2, bottom, where the effects of the ALP momentum cut and the typical signal selection efficiency are included. As evident in this figure, with the current dataset, FASER has the sensitivity to see hundreds of ALP events in currently unconstrained regions of parameter space. Also shown is a contour highlighting

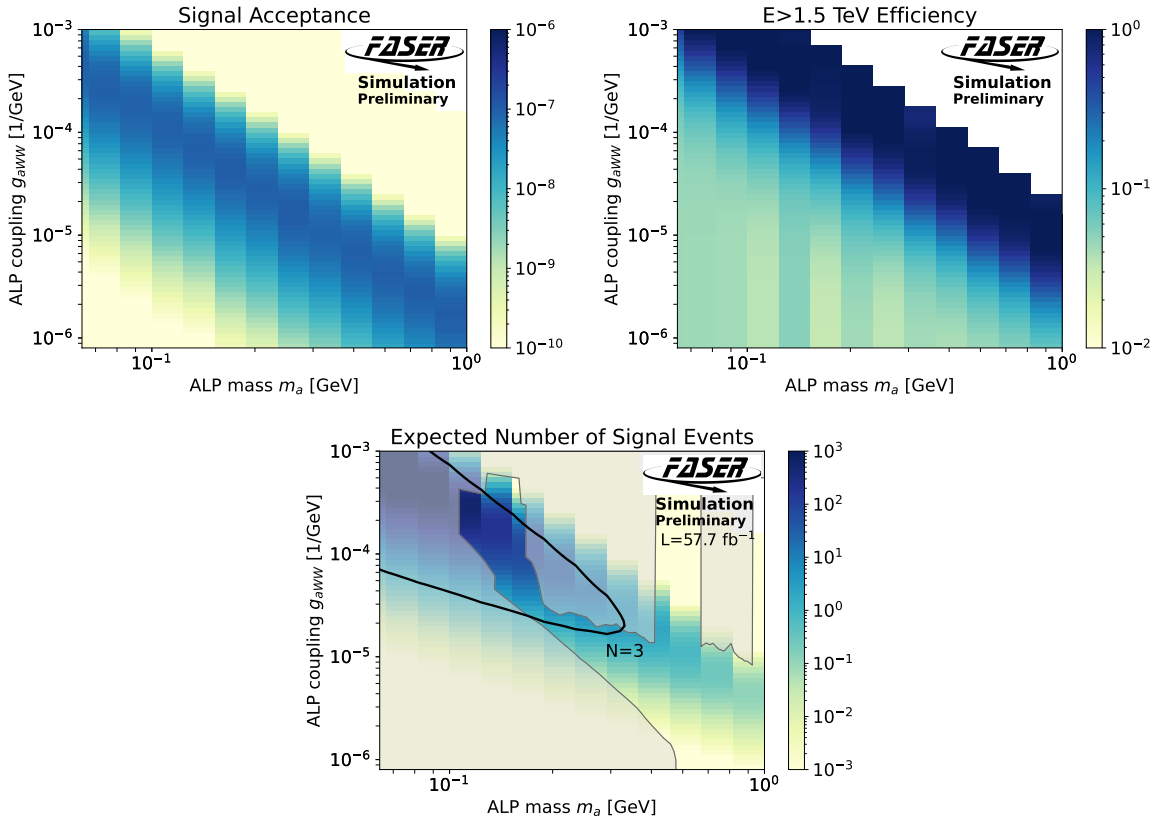

FIG. 2. The acceptance for events from the ALP model at truth level to decay inside FASER (top left). The efficiency of selecting ALP events in FASER with ALP energies above 1.5 TeV (top right). Expected number of ALP signal events in FASER, assuming 57.7 fb^{-1} and accounting for the typical signal selection efficiency on top of a 1.5 TeV energy requirement (bottom). Shaded areas highlight previously excluded parameter space.

the region with more than three expected signal events, which indicates that previously unexplored parameter space with masses $m_a \sim 60$ MeV $-$ 400 MeV and couplings $g_{aWW} \sim 10^{-5} - 10^{-3}$ GeV^{-1} are expected to be probed by FASER.

III. THE FASER DETECTOR

The FASER experiment, described in detail in Ref. [4], is located in the TI12 connection tunnel, close to the Super Proton Synchrotron (SPS) and about 5 m away from the LHC. It is aligned with the LOS of the IP1 collision axis.[1] However, due to the crossing angle in IP1, the LOS is offset vertically by 6.5 cm with respect to the centre of the detector, which is properly accounted for in the simulation. With a 10 cm-radius active transverse size, it covers an angular acceptance corresponding to a pseudorapidity $\eta > 9.2$ around the LOS with respect to IP1.

The detector (see Figure 3) consists of a front scintillator veto system, the FASERν emulsion

[1] FASER uses a right-handed coordinate system. The origin of the coordinate system in the transverse plane is the centre of the detector axis. In the longitudinal direction, the origin is at the front of the first tracking station of the spectrometer, which is 477.759 m from IP1. The x-axis points horizontally towards the center of the LHC, the y-axis vertically towards the Earth's surface, and the z-axis along the central detector axis, away from IP1. A radial variable based on the x and y coordinates can be defined, with the azimuthal angle ϕ around the z-axis. Pseudorapidity is $\eta = -\ln\tan(\theta/2)$, where θ is the angle relative to the LOS.

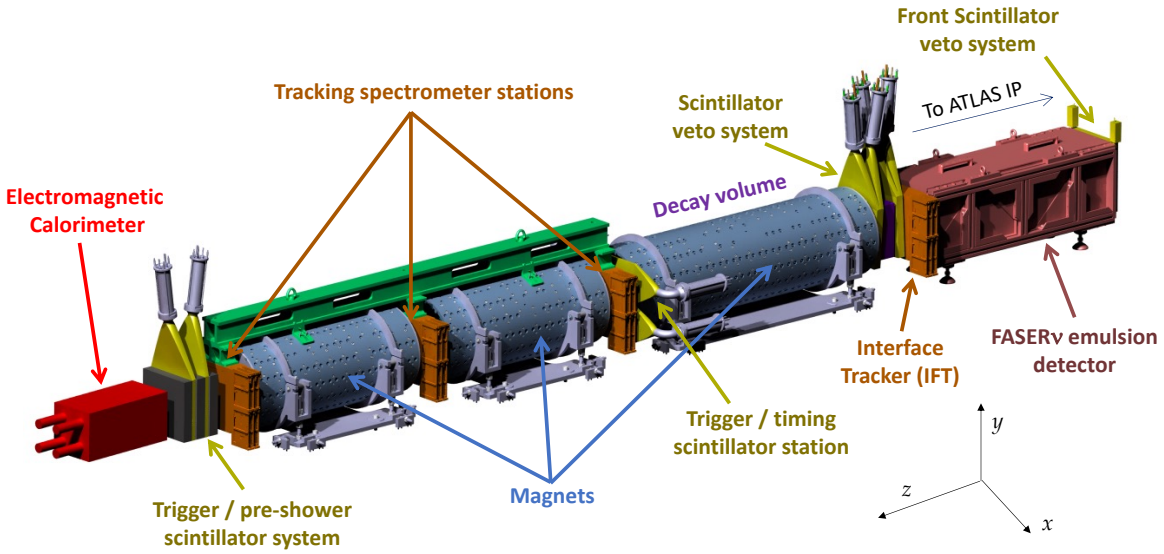

FIG. 3. A sketch of the FASER detector, showing the different detector systems. The detector coordinate system is also shown [4].

detector, the interface tracker (IFT), the FASER scintillator veto station, the decay volume, the timing scintillator station, the FASER tracking spectrometer, the preshower scintillator system, and the EM calorimeter system. The detector includes three 0.57 T dipole magnets, one surrounding the decay volume and the other two embedded in the tracking spectrometer. The key components of interest for this analysis include the three magnets, the scintillator (including the preshower) system, and the EM calorimeter.

The scintillator system includes four stations, each featuring multiple scintillator counters as follows:

- Towards the front of the detector is the VetoNu station, comprising two scintillator counters positioned in front of the FASERν tungsten/emulsion detector. While the FASERν detector is not utilized in this analysis, the eight interaction lengths of tungsten play a role in suppressing potential backgrounds.
- In front of the decay volume is the veto scintillator station composed of three scintillator counters, with a 10 cm-thick lead absorber placed between the two downstream scintillators and the upstream one.
- For triggering and timing measurements and as an additional veto layer, the timing scintillator station is placed after the decay volume and in front of the tracking spectrometer. This station consists of two scintillator counters separately covering the top and bottom half of the detector (with a small overlap region in between). The scintillators are 1 cm thick to minimize the material in the detector volume. The timing scintillators cover a bigger transverse area (40 cm $\times$ 39 cm) with respect to the LOS, which allow to tag incoming large angle muons that miss the veto scintillators and could lead to a large energy signal in the calorimeter.
- A preshower detector, consisting of two scintillator layers, is placed after the tracking spec-

trometer and in front of the calorimeter. Both modules are preceded by a 3 mm-thick layer of radiator (tungsten) to create a simple preshower detector. The purpose of the preshower is to differentiate between an incoming EM shower formed by an incoming high-energy photon and a neutrino interacting in the calorimeter material. To reduce backsplash from the calorimeter and preshower radiator into the last tracking station, a 5 cm-thick graphite plate is placed in front of each layer of tungsten and between the final scintillator module and the calorimeter.

All scintillators (except the preshower) are used to veto events with incoming charged particles, which are mostly muons.

Since the signal of interest is not relying on the reconstruction of tracks through the tracking spectrometer (see Section V), the analysis is sensitive to ALPs decaying within an extended decay volume comprising the region between the veto scintillators and the preshower scintillator station (referred to as the sensitive detector volume in the following).

The EM energy of particles traversing the detector volume is measured by the EM calorimeter located at the furthest end of the detector. The calorimeter is composed of four spare modules from outer ECAL of the LHCb experiment [19], each comprising a total depth of 25 radiation lengths. The energy resolution has been measured to be $\mathcal{O}(1\%)$ [4] in the high energy range most relevant for this analysis using data collected in the testbeam at the CERN SPS carried out in July 2021.

Events are triggered by signals from the scintillators or calorimeter system, with a typical trigger rate of 1 kHz. This is dominated by high-energy muons entering FASER from collision decay products in IP1. The average detector deadtime was measured to be 1.3%. The trigger and data acquisition system is described in more detail in Ref. [20]. In this analysis, the calorimeter trigger is used and is fully efficient for energy deposits above 20 GeV.

IV. DATA AND SIMULATION SAMPLES

Data events collected during 2022 and 2023 in $\sqrt{s} = 13.6$ TeV collisions provided by the LHC during its ongoing Run 3 data-taking are used. The dataset analysed corresponds to an integrated luminosity of 57.7 fb^{-1}. The ATLAS luminosity measurements and calibrations described in Refs. [21–23] are used.

A set of 55 ALP signal MC samples spanning the mass-coupling parameter space are generated with `FORESEE`. Uncertainties based on flux modelling are considered through generator variations. The decay of ALPs up until the preshower layer is simulated within a 100 mm radius of the detector axis. The simulation of forward B-mesons follows the latest prescription developed in Ref. [24], using `POWHEG` [25–27] with the NNPDF3.1sx+LHCb PDF set [28, 29] to model B-meson production at NLO+NLLx accuracy, matched with `Pythia 8.3` [30] to model the parton shower and hadronization. The uncertainties taken into account on the B-meson production rates are flux uncertainties based on variations of the renormalization and factorization scales. The kaon decay rate prediction is based on `EPOS-LHC` [31], with `SIBYLL` 2.3d [32], `QGSJET 2.04` [33], `Pythia` [34] and `PYTHIAforward` [35], a dedicated forward physics tune of `Pythia`, used as alternative MC generators to estimate the corresponding flux uncertainty.

For background studies, described in detail in Section VI, various MC samples are used. Neutrinos are produced upstream of FASER through light- and charm-hadron decays and can then undergo charged- and neutral-current interactions in FASER. The neutrino fluxes were obtained using the fast neutrino flux simulation presented in Ref. [36], with adjustments made to match the LHC's configuration during Run 3 [37]. Following the recommendations detailed in Ref. [37], the central prediction for the neutrino flux from light hadrons is based on `EPOS-LHC`, with systematic uncertainties estimated by the spread of generator predictions from `SIBYLL`, `QGSJET` and

PYTHIAforward. For charm hadrons, the POWHEG+Pythia [24, 26] prediction is used, with uncertainties from scale variations. Neutrino events interacting in FASER are simulated with GENIE [38–40]. For each of the nominal samples and variations, 10 ab^{-1} are simulated. The Bodek-Yang model [41–43] employed in GENIE agrees with more recent cross section models [44, 45] to within $\leq 6\%$ over the range of energies of interest [37]. Two dedicated high-energy muon simulation samples are used to aid in the evaluation of neutral-hadron and large-angle muon backgrounds (see Section VI), both employing the simulated energy and angular distributions from FLUKA [46–48]. The FLUKA setup includes a realistic modelling of the LHC infrastructure between IP1 and FASER, and has been validated by comparisons to LHC data. The first sample has 15M events of muons entering FASER from IP1. The second sample considers muons generated upstream of the front scintillator veto stations, with a radius of 9–25 cm, and includes 400k muon events. Additional muon simulation samples are used for studies evaluating systematic uncertainties.

On top of the various event simulations listed above, GEANT4 [49] is used to simulate the particle propagation and interactions within the FASER detector. It includes a realistic detector geometry, including passive material. An additional 8.8% correction factor is applied to the calorimeter EM energy based on testbeam studies, aligning the calibrated MC energy with the testbeam data, following the procedure of Ref. [10]. Correction factors are also evaluated for the simulated response of the preshower, both in terms of the second preshower charge deposit, measured in terms of energy deposit of a minimum ionising particle (MIP) or MIP-equivalent (nMIP), and the preshower (PS) ratio, defined as the ratio of the number of MIP equivalent charge in the second preshower layer compared to the first preshower layer. Photon conversion events from FASER data as well as single-particle electron events from testbeam data are used. The correction factors are estimated through fitting the deposited energy distributions for each layer and extracting the most probable value for data and MC. The latter are then corrected to match the data. The correction factors are 1.20 and 1.13 for the second preshower layer nMIP and the PS ratio, respectively, and show no dependence on the energy. These preshower correction factors are evaluated in FASER data, with the difference relative to their values in the testbeam data used as uncertainty, as discussed in Section VII.

V. EVENT SELECTION AND RECONSTRUCTION

The reconstruction of data events recorded in FASER uses the Calypso [50] framework, based on the open-source ATLAS athena reconstruction software [51, 52]. The total charge of the calorimeter and scintillator signals is extracted by summing the digitised pulse values post-pedestal subtraction. Simulation samples follow the same reconstruction as data.

The typical signature of a signal event in the detector is shown in Figure 4 and can be summarised as:

- No signal is observed in the veto scintillators, since ALPs are electrically neutral.
- Preshower charge deposits[2] consistent with an EM shower arising from the decay photons.
- A large energy deposit in the calorimeter left by the high-energy photon pairs.

To avoid any bias in the analysis, a blinding methodology was implemented. A "blinded" region was defined as events with a limited deposited charge in any of the veto scintillators and calorimeter energy surpassing 100 GeV. Event selection, background estimation, and the consideration of systematic uncertainties were all concluded prior to investigating this blinded region.

[2] A charge deposit is defined as the measured charge in the photomultiplier tube (PMT) when particles lose energy and generate light in the scintillators.

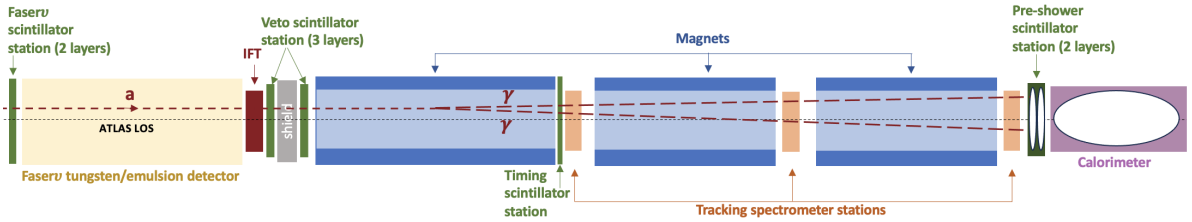

FIG. 4. Sketch of an ALP event traversing through the FASER detector. As ALPs are electrically neutral, we expect no signature in any of the veto stations, followed by signal in the preshower and large deposit in the calorimeter. The dotted lines show that the ALP is leaving no signal in the detector and the white blobs in the preshower layers and the calorimeter depict energy deposits. The ALP is allowed to decay within the sensitive detector volume comprising the region across all three magnets, with a total length of 4 m.

Following the above, the event selection requires events triggering the calorimeter and in time with the collision timing. Hence, only events corresponding to colliding bunches are selected, with a requirement on the calorimeter timing to be > -5 ns and < 10 ns to ensure consistency with collision timing. These times are with respect to the expected time, and are calibrated on a run-by-run basis using muon events.

Since no veto signal is expected from the ALPs signal, the charge deposited in each of the five veto stations is required to be less than half that expected from a MIP.

With the current detector design, the two photons cannot be resolved and hence selections on the overall charge deposits in the preshower and calorimeter are applied. A charge deposit is required in the preshower layers, with the second layer being greater than the charge deposit equivalent of 10 MIPs and the preshower ratio being greater than 4.5. This is because the photons are expected to shower in the material in the preshower, releasing more energy in the second layer, hence the preshower ratio is expected to be high. Lastly, a large calorimeter energy deposit above 1.5 TeV is required for the two-photon ALP signature. For this analysis, the calorimeter energy variable considered is the summed calorimeter energy across all modules.

The selections applied on data and MC are summarised in Table I. The event selection is designed to ensure high acceptance of ALPs that decay anywhere in the sensitive detector volume, ALPs decaying inside the calorimeter will be suppressed by the preshower cuts. Additionally, the two photons from the ALP decay are generally separated by < 1 mm and the detector resolution cannot resolve this. To increase sensitivity to such models, an upgrade to the preshower system is planned [53].

Cutflows showing the fraction of events that pass the above selection are shown in Table II for a representative ALP model. Across the (m_a, g_{aWW}) parameter space in regions FASER is sensitive to, the efficiency of the preshower ratio cut is between 75 and 80%. Across the ALP mass range the efficiency of the second preshower layer cut is above 95%. The efficiency of the calorimeter energy cut for low mass and high coupling is close to 99%, and at higher mass the efficiency is between 30% and 90%. At low mass and low coupling this falls to less than 30%, but this region is already largely excluded.

VI. BACKGROUND ESTIMATION

Various sources of background are considered in the analysis. The primary background is anticipated to result from neutrino interactions within the detector. Other physics-related backgrounds may arise from neutral hadrons entering the detector, muons that bypass the veto scintillator

Trigger and Data Quality
Selecting events with calorimeter triggers
Calorimeter timing (> -5 ns and < 10 ns)
Baseline Selection
Veto/VetoNu Scintillator to have no signal (< 0.5 MIPs)
Timing Scintillator to have no signal (< 0.5 MIPs)
Signal Region
Preshower Ratio to have EM shower in the Preshower (> 4.5)
Second Preshower Layer to have signal (> 10 MIPs)
Calorimeter to have a large deposit (> 1.5 TeV)

TABLE I. Selections used in the analysis.

Selection	Efficiency	Cum. Efficiency
$m_a = 140$ MeV, $g_{aWW} = 2 \times 10^{-4}$ GeV^{-1}		
Veto Signal nMIP < 0.5	99.6%	99.6%
Timing Scintillator Signal nMIP < 0.5	97.8%	97.4%
Preshower Ratio > 4.5	85.7%	83.5%
Second Preshower nMIP > 10	98.6%	82.3%
Calo $E > 1.5$ TeV	91.6%	75.4%

TABLE II. MC cutflow for a representative ALP signal point with $m_a = 140$ MeV and $g_{aWW} = 2 \times 10^{-4}$ GeV^{-1}, showing the percentage of signal events passing each cut. A cut on the calorimeter energy > 20 GeV is used to emulate the effect of the calorimeter trigger in MC, and the efficiencies stated are relative to this emulation.

systems as they enter the detector at an angle, or veto inefficiencies. Additionally, non-collision backgrounds originating from cosmic rays or beam-related events are also taken into account. The following subsections provide a detailed description and quantification of the main source of background due to neutrino interactions as well as evaluations and checks of the other, ultimately negligible, background sources.

A. Neutrino Background

Neutrinos are produced upstream of FASER through light and charm hadron decays and can then undergo charged and neutral current interactions in FASER. They will evade FASER's veto stations but interact in or near the preshower or the calorimeter, resulting in a possibly significant background contribution due to minimal upstream activity, resembling signal events.

This background is evaluated in MC simulations (see Section IV) and validated in regions designed to target neutrinos interacting in different areas of the detector. The MC predictions for the number of signal events in 57.7 fb^{-1} in the signal region are summarised in Table III. The number of events originating from light and charm hadrons are shown together with their flux uncertainties. These systematic uncertainties are in general asymmetric, and so when combined they are first symmetrised by taking the maximum absolute variation from the nominal.

As described in Section V, only small charge deposits are expected in the Veto, VetoNu, and Timing Scintillators for an ALP decaying in FASER. The neutrino background is therefore studied

> 1.5 TeV signal region	
Light	$0.23^{+0.01}_{-0.11}$ (flux) $\pm$ 0.11 (exp.) $\pm$ 0.04 (stat.)
Charm	$0.19^{+0.32}_{-0.09}$ (flux) $\pm$ 0.06 (exp.) $\pm$ 0.03 (stat.)
Total	**0.42 $\pm$ 0.38 (90.6%)**

TABLE III. Summary of the MC estimate of the neutrino background in the signal region. Uncertainties on the flux, as well as experimental uncertainties further discussed in Section VII, are also given. The MC events are normalised to 57.7 fb^{-1} and MC statistical uncertainties are given.

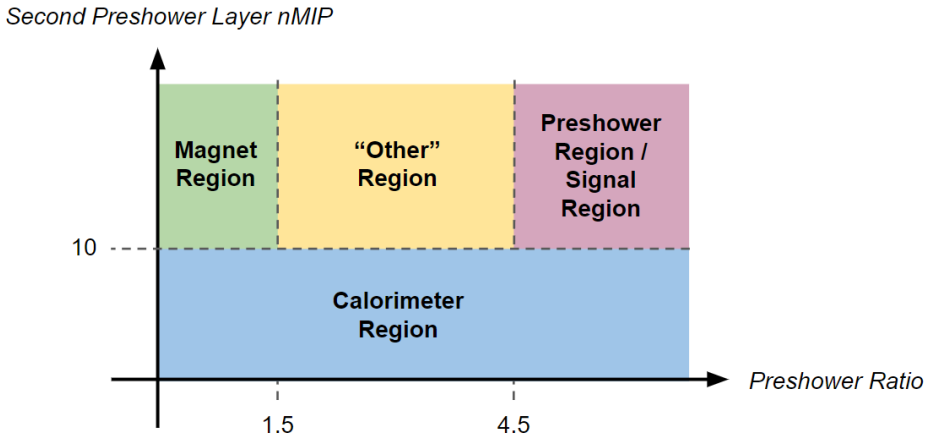

FIG. 5. Schematic of the regions used in the analysis. The 1.5 TeV signal region is a high-energy subset of the preshower region, with an additional energy requirement of at least 1.5 TeV.

after the baseline selection requirements on those charge deposits described in Table I.

Imposing requirements on the preshower variables has been shown to provide selection power among neutrinos interacting in different parts of the detector. Effective distinction between neutrinos interacting in the magnet, calorimeter, and preshower is achieved through selections on the charge deposited in the second preshower layer and the ratio of deposits of the two preshower layers. Neutrinos interacting in the magnet material deposit high charges in the second preshower layer and have a PS ratio around one, whereas neutrinos interacting in the calorimeter material deposit lower charges in the second preshower layer and have a broader PS ratio range. Those interacting in the preshower material closely resemble signal events, posing a challenging background. Three regions are therefore defined on the basis of the above categorization, as illustrated in Figure 5. A fourth region, labelled as "Other", is in between the calorimeter and magnet regions with PS ratio between 1.5 and 4.5. In the design of the validation regions, particularly the magnet and calorimeter regions, signal contamination was taken into account and is below 30% for the ALP parameter space not previously excluded.

Figure 6 shows the distribution of the location of the neutrino interaction vertex in the (z, r) plane in simulation, as well as the decay vertex of a representative ALP signal model with $m_a = 120$ MeV and $g_{aWW} = 10^{-4}$ GeV^{-1}. The radius $r = \sqrt{x^2 + y^2}$ is the distance from the central detector axis. Events with a minimum calorimeter energy deposit of 100 GeV are shown in the left column of Figure 6, and events with a larger than 1 TeV energy deposit in the right column. Neutrinos of both electron and muon flavour can be seen interacting throughout the detector volume, in particular in detector areas with larger material density such as the magnet, preshower scintillator system, and the calorimeter. The calorimeter region is shown in the first row of Figure 6,

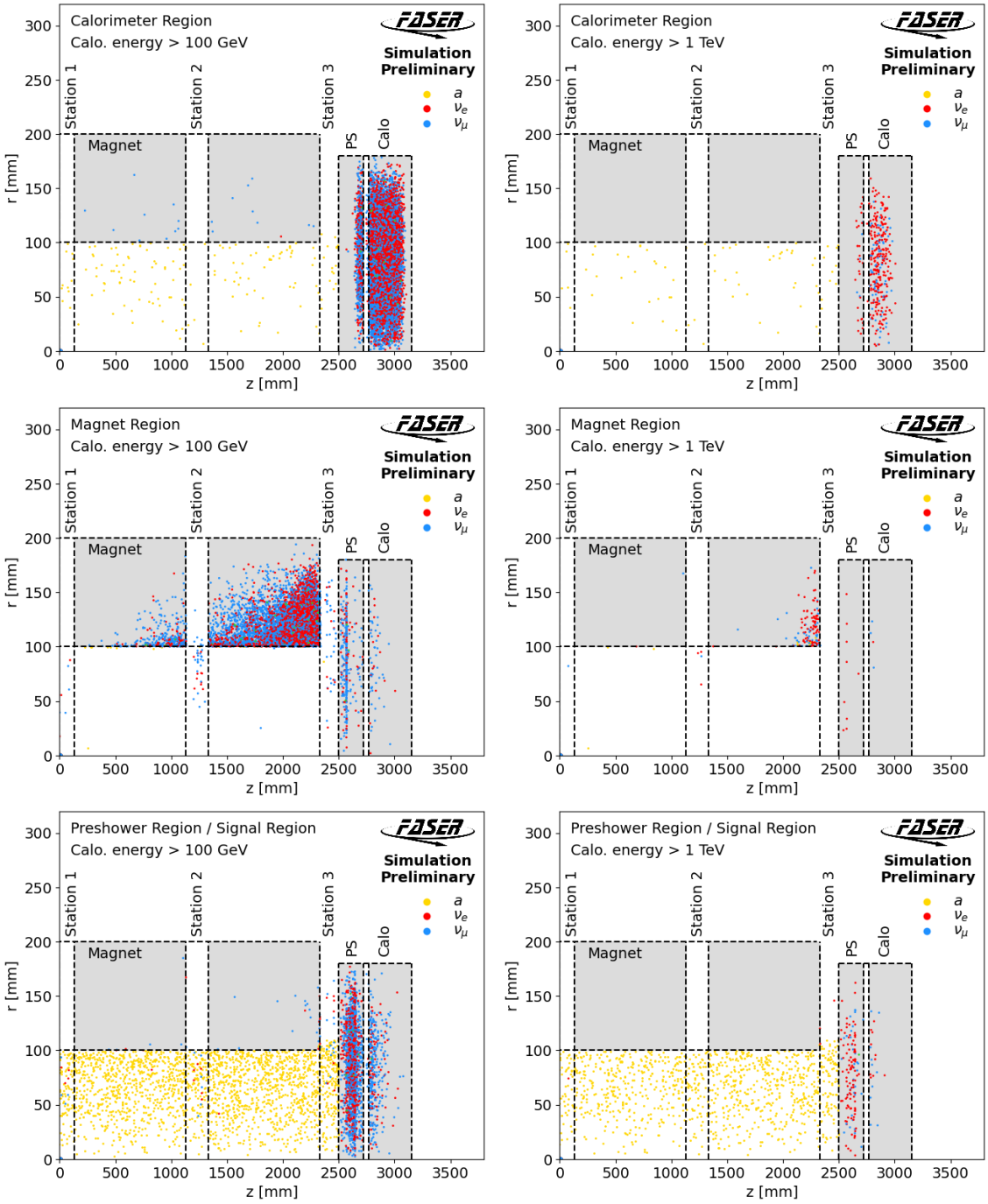

FIG. 6. Distributions in (z, r) plane of the neutrino (ALP) interaction (decay) vertex within the FASER detector for the different regions with different requirements on the calorimeter energy.

clearly favouring neutrinos interacting within the calorimeter volume. In the second row of Figure 6, the background composition in the magnet region is given. The last row highlights the preshower and signal regions, dominated by neutrinos interacting in the preshower and, at higher energies, dominated by ALP decays.

The magnet and calorimeter regions show high efficiency ($> 80\%$) and purity among neutrino

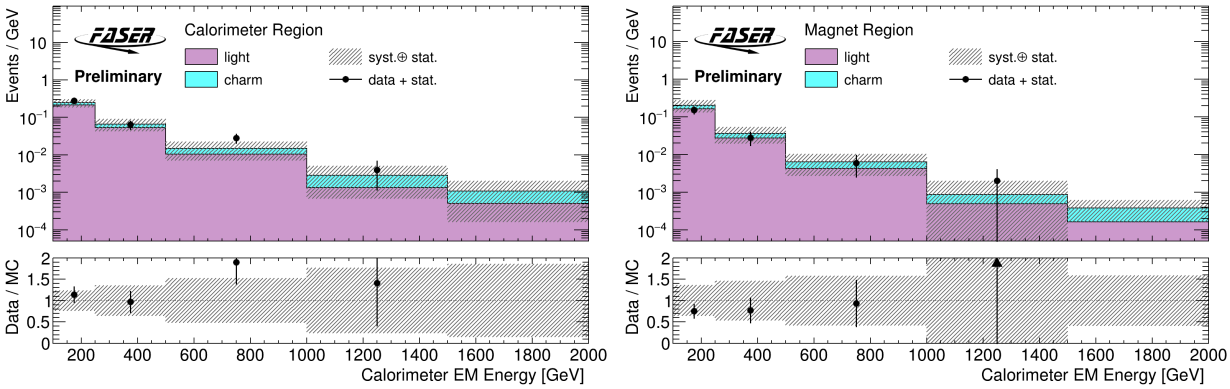

FIG. 7. Calorimeter energy distributions in the calorimeter (left) and magnet (right) region. The uncertainty band includes MC statistical uncertainties, experimental uncertainties, and uncertainties on the neutrino background flux. The last bin contains all events above 1.5 TeV. Equivalent distributions split by neutrino flavour can be found in Appendix 4.

events ($> 90\%$) for selecting true neutrinos interacting in the magnet and calorimeter, respectively. However, the preshower region's efficiency is $< 40\%$, with most rejected preshower neutrinos falling into the "Other" and calorimeter regions.

Table IV shows the observed number of data events in each validation region, as well as the expected neutrino contribution, split in terms of their origin from light and charm hadron decay, as predicted by MC. The MC describes the data well in all regions within statistical and systematic uncertainties, the latter dominated by the uncertainty on the flux modelling. A breakdown of the composition by neutrino flavour can be found in Appendix 4.

Figure 7 shows the energy distribution in the calorimeter region and the magnet region, comparing data to MC predictions. The calorimeter region is dominated by muon neutrinos, particularly at lower energies. The magnet region is dominated by neutrinos produced in light hadron decays, showing good agreement between data and MC within uncertainties. The preshower region most closely emulates the neutrino event topologies in the signal region, serving as additional validation of the background modelling. The high-energy tail includes the signal region, and it is shown and further discussed in Section VIII.

B. Other Background Contributions

Veto System Inefficiency One source of background events is muons traversing the detector volume. FASER's veto system prevents significant amounts of muons from contaminating the regions of interest. Possible inefficiencies of each of the five veto scintillators are assessed using data by specifically choosing events with one well-reconstructed track. For each individual plane, the inefficiency is determined by counting the proportion of events where the scintillator charge falls below the 40 pC threshold, reflecting half the charge from a MIP crossing the scintillator. This background can be considered to be negligible based on the measured per-layer inefficiencies of the scintillators below 10^{-5} and an expected number of muons of the order of 10^{8}. It has been assumed that the scintillator inefficiencies are uncorrelated.

Background from Large-Angle Muons Muons traversing the detector volume at a large angle might miss the veto system, interact, and deposit high energy within the calorimeter. Unlike

Magnet region	
Light	$33.6^{+6.7}_{-3.4}$ (flux) ± 4.3 (exp.) ± 0.4 (stat.)
Charm	$9.9^{+16.1}_{-4.6}$ (flux) ± 0.9 (exp.) ± 0.2 (stat.)
Total	**43.5 ± 18.2 (41.9%)**
Data	**34**
"Other" region	
Light	$17.4^{+1.3}_{-0.8}$ (flux) ± 2.5 (exp.) ± 0.3 (stat.)
Charm	$3.9^{+6.0}_{-1.8}$ (flux) ± 0.5 (exp.) ± 0.2 (stat.)
Total	**21.3 ± 6.9 (32.2%)**
Data	**17**
Calorimeter region	
Light	$51.6^{+2.0}_{-3.4}$ (flux) ± 3.1 (exp.) ± 0.5 (stat.)
Charm	$11.1^{+19.1}_{-5.1}$ (flux) ± 0.4 (exp.) ± 0.3 (stat.)
Total	**62.7 ± 19.7 (31.4%)**
Data	**74**
Preshower region	
Light	$14.8^{+0.9}_{-1.2}$ (flux) ± 1.8 (exp.) ± 0.3 (stat.)
Charm	$3.0^{+4.5}_{-1.4}$ (flux) ± 0.3 (exp.) ± 0.1 (stat.)
Total	**17.8 ± 5.1 (28.8%)**
Data	**15**

TABLE IV. Breakdown of the neutrino composition and data yields in the Magnet, "Other", Calorimeter and Preshower regions (excluding events passing signal region selections). Listed are data and neutrino yields as predicted from MC in 57.7 fb^{-1}, also split in light and charm production components. Uncertainties on the flux as well as experimental uncertainties further discussed in Section VII are also given.

in the search for dark photons [10], there are no requirements for tracks associated to the muon that can be used to veto such background, hence several checks are performed on MC and data to ensure it is heavily suppressed and therefore negligible. Dedicated MC samples have been produced (see Section IV) of muons traversing FASER using `FLUKA`. No events pass the selections applied. A partially data-driven approach has been investigated to validate the MC results, using events with an inverted timing scintillator charge selection and inverted PS-ratio selection and calorimeter energy above 100 GeV. Nonetheless, contributions from neutrino interactions background, subtracted using MC predictions, are the dominant component in all regions considered, leading to a fraction of large-angle muons candidate events below 5% in the region below 200 GeV, and negligible above 200 GeV, as predicted by MC estimates. Visual checks on the few remaining data events in validation regions with high-energy calorimeter deposits confirm they are consistent with neutrino interaction events.

Neutral Hadron Background Background from neutral hadrons generated in muon interactions within the rock in front of FASER may occur if these neutral hadrons pass through the veto system and subsequently interact or decay within the detector decay volume, resulting in signal in the preshower and a high calorimeter energy deposit. The likelihood of this background is significantly reduced by the requirements that the neutral hadron traverse the entire eight interaction lengths of the FASERν detector and that the parent muon scatter in a way that avoids the veto scintillators. Additionally, the high calorimeter energy requirement supresses the neutral

hadron background further. In the dark photon analysis [10], the estimate of the neutral hadron background passing the analysis selections was found to be negligible. In the current analysis, the veto scintillator requirements are the same, and the calorimeter energy requirement is 1.5 TeV compared to 500 GeV in the dark photon analysis. Hence, such backgrounds are considered negligible.

Non-Collision Background For non-collision background studies, events were collected during periods without colliding bunches in IP1. Cosmic data worth 33 days of beam-free data-taking were examined, equivalent to the full 2022 and 2023 physics data-taking duration. No events with calorimeter energy deposits exceeding 100 GeV were observed and only 9 events, irrespective of energy, pass the baseline selections outlined in Table I, indicating the negligible impact of cosmic-ray events when considering other analysis requirements.

Beam background from LHC Beam 1 (B1), the incoming beam to ATLAS in the FASER location, is the most relevant for FASER. Potential detector activity arises from beam-gas interactions or beam tails interacting with the beampipe aperture, resulting in particles directed towards FASER with limited shielding. Low-energy activity can be observed in FASER correlated with B1 bunches passing the back of the detector, 127 bunch-crossings before particles from the collisions of the same bunch would be recorded in FASER. This beam background is studied by checking the detector activity in events with bunch crossing identifiers corresponding to proton bunches in LHC B1 passing the back of FASER, but which do not correspond to colliding bunches at IP1. Despite observing events with no signal in the veto scintillators and timing scintillators, beam background is suppressed to a negligible level when calorimeter timing selections are applied. Studies of collision timing and beam background show that the timing of such B1 events and collision events are well separated. The timing cut outlined in Section V effectively removes all B1 background. As a result, the overall contribution from non-collision backgrounds, including cosmic rays and beam background, is deemed negligible.

VII. SYSTEMATIC UNCERTAINTIES

Systematic uncertainties arise from various sources and have an effect on both expected signal yields and background estimates.

The largest source of uncertainty that affects signal yields is the uncertainty associated with the modelling of the flux of SM particles produced in the forward direction of the LHC, from which the ALP is produced [24, 35]. Uncertainties on the production of B-mesons are derived from the effect on the signal yield of each generator, compared to the "central value" provided by the `POWHEG+PYTHIA` prediction. The shift in the yields for each component is added in quadrature. An additional 20% uncertainty, to account for uncertainties in the modeling of the $B \to X_s a$ branching ratio [24], is also included in this signal systematic. These flux uncertainties have an effect on the signal yields of between 30 to 60%, depending on the ALP mass and coupling.

The experimental uncertainties on the signal yields arise from the modelling of the detector response in the MC simulation. The uncertainty on the calorimeter energy scale calibration is evaluated following the procedure used in Ref. [10] that considers the difference in the calibration of the energy scale between data and MC simulation, and it is quantified as around 6% across the energy range of interest. The systematic uncertainties on the correction factors for the second preshower layer MIP-equivalent charge deposit and PS ratio are evaluated considering the difference of the factors obtained with FASER and the testbeam data and is 20% for second preshower layer

Signal Sample	Flux	Stat.	Luminosity	Calorimeter	Second Preshower Layer	Preshower Ratio
$m_a = 140$ MeV $g_{aWW} = 2 \times 10^{-4}$ GeV^{-1}	59.4%	1.8%	2.2%	3.6%	0.6%	7.9%
$m_a = 120$ MeV $g_{aWW} = 10^{-4}$ GeV^{-1}	57.3%	3.5%	2.2%	16.3%	0.6%	6.9%
$m_a = 300$ MeV $g_{aWW} = 2 \times 10^{-5}$ GeV^{-1}	58.0%	2.9%	2.2%	15.8%	0.6%	8.4%

TABLE V. The various sources of systematic uncertainties associated with the signal. Theory uncertainties include the uncertainty associated with the flux and the statistical uncertainty. Experimental uncertainties include the uncertainty on the luminosity, the calorimeter energy, the second preshower layer charge and the preshower ratio. These are shown for three ALP MC signal points: $m_a = 140$ MeV, $g_{aWW} = 2 \times 10^{-4}$ GeV^{-1}; $m_a = 120$ MeV, $g_{aWW} = 10^{-4}$ GeV^{-1}; and $m_a = 300$ MeV, $g_{aWW} = 2 \times 10^{-5}$ GeV^{-1}.

and 13% for the PS ratio. The resulting effect on the yields is evaluated as a shift in the respective parameter values used in region definitions and is of the order of 1% and 5%, respectively. All above mentioned uncertainties were evaluated for each signal point in the ALP parameter space. Overall, experimental uncertainties on the calorimeter energy scale and preshower-related quantities are $\mathcal{O}(30\%)$.

The luminosity uncertainty was taken from ATLAS for the 2022 data [21–23]; it is quoted to be 2.2% and is assumed to be the same for 2023 data. The statistical uncertainty from the number of MC simulated signal events is also included and ranges from 1 to 2%.

Table V shows a break down of different theory and experimental systematics for three representative signal samples.

The main source of systematic uncertainty for the SM background arises from the theoretical modeling of the flux of neutrinos used to quantify the contributions due their interactions. The composition of neutrinos arriving in FASER originates from both light and charm hadron decays as described in Section VI. The main uncertainties related to the modelling of these neutrino events stem from the hadron flux uncertainty. To account for those, the prescription of generator and scale variations detailed in Ref. [37] was used. The overall impact on the background estimate for neutrino interactions is around 90%, inclusive of the uncertainty on the statistics of the MC samples used. The same experimental uncertainties as detailed for the signal above are also applied to the neutrino background MC.

VIII. RESULTS

The total background expectation in the signal region is summarised in Table VI. Also shown are the expected yields for three benchmark ALP models representative of the parameter space targeted by this analysis. One event is observed in the signal region, consistent with a background-only hypothesis and within 0.63σ of the SM expectation. This data event has a calorimeter energy of 1.6 TeV, a preshower ratio of 9.0, and charge deposit in the second preshower layer equivalent to 146 MIPs.

Figure 8 shows the neutrino background expectation in the preshower and signal regions, with uncertainty bands including the experimental and theoretical systematic uncertainties. To illustrate the possible signal contributions, three representative ALP signal predictions are overlaid. The signal region is dominated by electron neutrinos produced in light and charm hadron decays.

A statistical interpretation of the result has been performed following a profile likelihood estima-

Source	Event Rate
Neutrino Background	0.42 ± 0.32 (flux) ± 0.14 (calo. energy) ± 0.06 (PS ratio) ± 0.02 (PS 1 nMIP) ± 0.05 (stat.) **Total: 0.42 ± 0.38 (90.6%)**
ALP ($m_a = 140$ MeV, $g_{aWW} = 2 \times 10^{-4}$ GeV^{-1})	70.7 ± 42.0 (theo.) ± 6.4 (exp.) ± 1.3 (stat.)
ALP ($m_a = 120$ MeV, $g_{aWW} = 1 \times 10^{-4}$ GeV^{-1})	91.1 ± 52.2 (theo.) ± 16.2 (exp.) ± 3.2 (stat.)
ALP ($m_a = 300$ MeV, $g_{aWW} = 2 \times 10^{-5}$ GeV^{-1})	4.0 ± 2.3 (theo.) ± 0.6 (exp.) ± 0.1 (stat.)
Data	**1**

TABLE VI. Summary of the expected event rates for the neutrino background and three representative ALP models, along with the number of events observed in the experimental data. A breakdown of the different sources of experimental and theoretical systematic uncertainties is also provided.

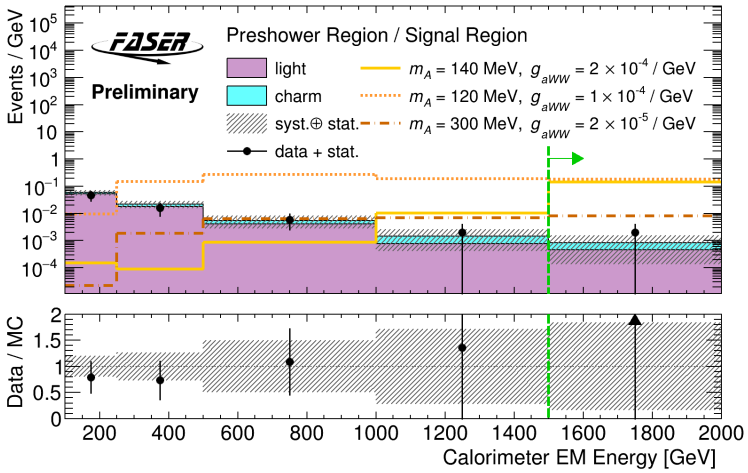

FIG. 8. Calorimeter energy distribution in the preshower and signal regions, showing the neutrino background composition separated according to neutrino production mechanism. The last high-energy bin above 1.5 TeV, highlighted with a green arrow, presents the signal region and includes the overflow. The neutrino background contributions, separated by neutrino flavour, are given in Appendix 4.

tion performed within the HistFitter statistical analysis framework [54]. Following a convention of evaluating the CL_s [55] values at 90% confidence level (C.L.), a contour encompassing the excluded parameter space in the ALP coupling versus mass plane is shown in Figure 9. Shown in grey are existing experimental limits from a wide range of experiments [14–16]. A detailed breakdown of the existing limits, shown in Figure 9 as joint excluded parameter space, can be found in Appendix 2.

For ALPs coupled to weak gauge bosons, FASER is sensitive to previously unexplored parameter space with ALP masses between 100 and 250 MeV and couplings ranging from 3×10^{-5} to 5×10^{-4} GeV^{-1}. ALPs as heavy as 300 MeV can be excluded for a coupling of 7×10^{-5} GeV^{-1}. A complementarity with kaon factory limits [15] is achieved for ALP masses below 100 MeV.

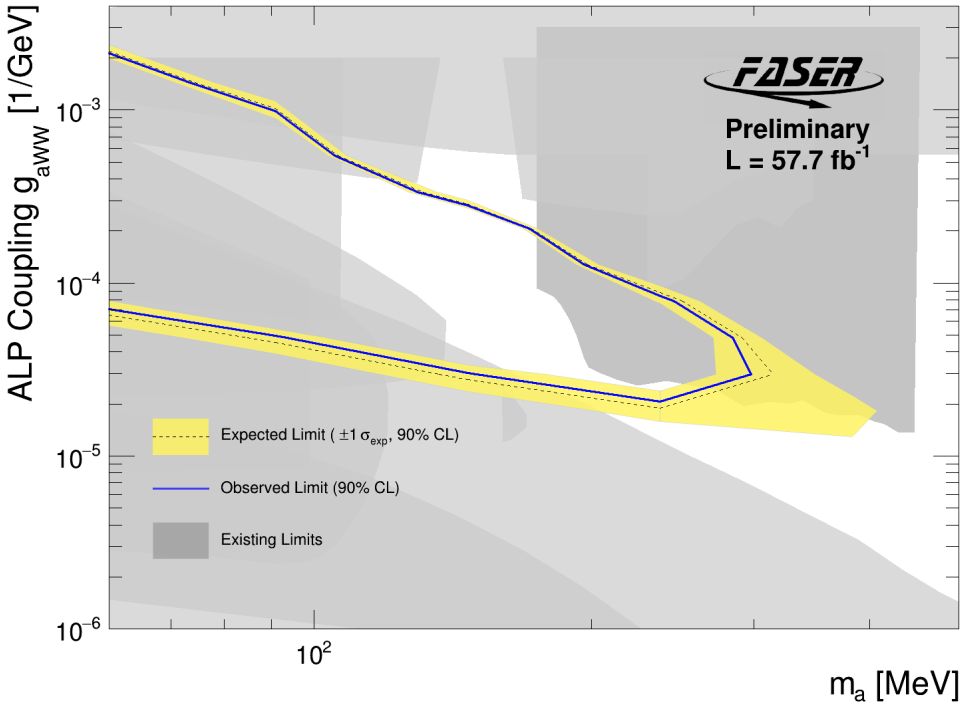

FIG. 9. Interpretation of the signal region yield as ALP exclusion limits with the assumption of 0.42 neutrino background events. Systematic uncertainties described in Table V are included.

IX. CONCLUSIONS

This note presents FASER's first search for new particles decaying into photons and ALPs, marking its first exploration of BSM physics predominantly produced in heavy-flavour decays. Data collected by FASER in 2022 and 2023 from proton-proton collisions at the LHC with a center-of-mass-energy of 13.6 TeV have been studied. A model with an ALP coupling to $\mathrm{SU}(2)_L$ gauge bosons has been considered. Multiple SM background sources that can mimic a similar detector signal as ALPs have been studied. The dominant background stems from neutrinos crossing the FASER detector volume and interacting with its material. Other backgrounds such as cosmic muons and interactions of the LHC beam with the beam gas have been studied and can be considered negligible in the context of this analysis. One data event was observed in the signal region, with a background expectation of 0.42 ± 0.38. Coupling strengths of the ALP to weak gauge bosons between 3×10^{-5} to 5×10^{-4} GeV^{-1} were excluded in previously unprobed parameter space with ALP masses between 100 and 250 MeV. ALPs as heavy as 300 MeV were excluded for a coupling strength of 7×10^{-5} GeV^{-1}.

APPENDIX

1. Scintillator Efficiencies in 2022 and 2023 Data

The scintillator efficiencies in the VetoNu and Veto layers as measured in 2022 and 2023 data in one-track events are given in Table VII.

Scintillator	2022	2023
Veto-0	99.999988(5)	99.999994(4)
Veto-1	99.999992(5)	99.999994(4)
Veto-2	99.999992(5)	99.999994(4)
NuVeto-0	99.99989(1)	99.99988(1)
NuVeto-1	99.99988(1)	99.99986(1)

TABLE VII. Veto scintillator efficiencies in a $R < 100$ mm fiducial region.

2. FASER ALP Limit in Relation to Previous Experiments

Figure 10 shows the observed ALP limit. Existing constraints are also shown from BaBar [56], SN1987 [57], E137 [58], LEP [59], E949 [60, 61], KOTO [62], KTeV [63], NA62 [64], NA48/2 [65], and CDF [66].

3. Event Display

The data event, here named the *ALPtrino* event, observed in the signal region is visualised through its detector signature in Figure 11.

4. Neutrino Compositions by Flavour

A breakdown by flavour composition of the neutrino background in the signal region, as well as in the Calorimeter, Magnet, "Other," and Preshower regions, is given in Table VIII. Figure 12 shows the energy distribution in the calorimeter and magnet region. Figure 13 shows the energy distribution in the preshower and signal region.

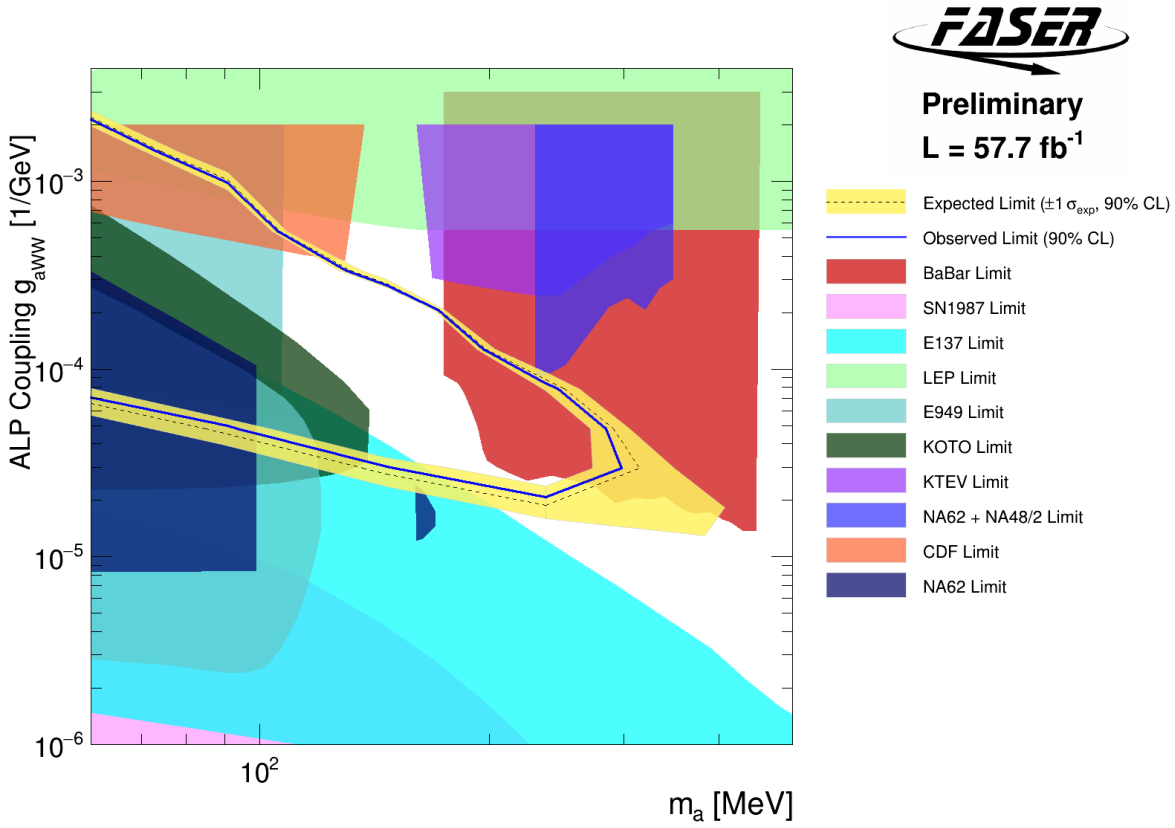

FIG. 10. Interpretation of the signal region yields as ALP exclusion limit, assuming 0.42 background events from the neutrino estimate. All systematic uncertainties described in Section VII are included. This figure shows the individual limits from other experiments.

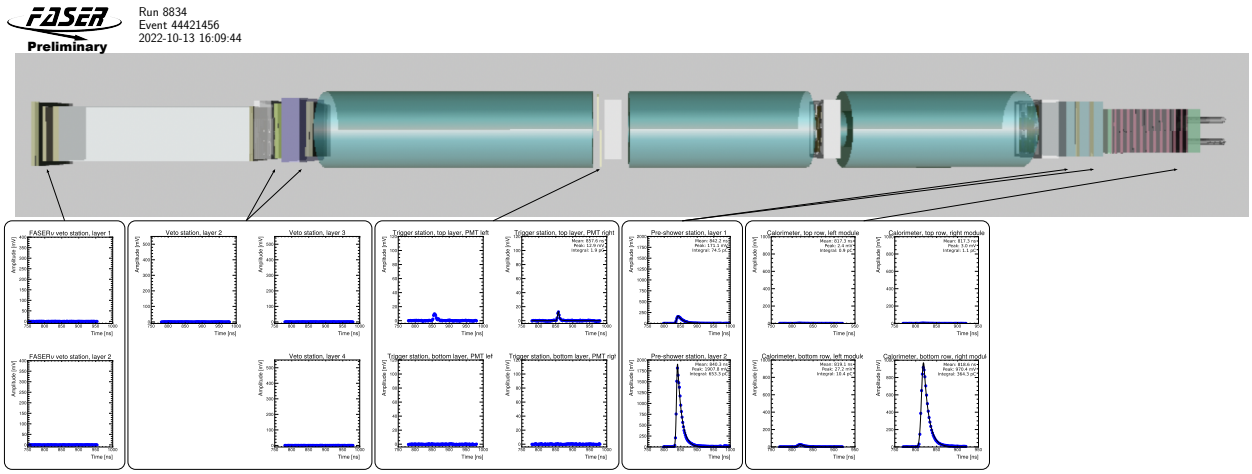

FIG. 11. Event display of the ALPtrino event recorded by FASER on 13 October 2022 with 13.6 TeV stable beams. The waveforms for signals in the scintillators and calorimeter modules are shown in blue, fitted to a Crystal Ball function. A clear signal in the second preshower layer equivalent to 146 MIPs can be seen. The event has been triggered by the calorimeter modules, with an overall reconstructed energy of 1.6 TeV. The ATLAS interaction point is 480 m to the left of the detector shown. In the title of the waveform plots, left and right is defined facing the downstream direction.

SR	
ν_e	0.32 ± 0.31 (flux) ± 0.10 (exp.) ± 0.04 (stat.)
ν_μ	0.09 ± 0.04 (flux) ± 0.05 (exp.) ± 0.02 (stat.)
Total	**0.42 ± 0.38 (90.6%)**
Data	1
Preshower region	
ν_e	5.16 ± 2.59 (flux) ± 0.51 (exp.) ± 0.17 (stat.)
ν_μ	12.6 ± 2.3 (flux) ± 1.61 (exp.) ± 0.3 (stat.)
Total	**17.8 ± 5.1 (28.8%)**
Data	**15**
Calorimeter region	
ν_e	22.6 ± 12.8 (flux) ± 0.7 (exp.) ± 0.4 (stat.)
ν_μ	39.9 ± 6.8 (flux) ± 2.8 (exp.) ± 0.5 (stat.)
Total	**62.7 ± 19.7 (31.4%)**
Data	74
Magnet region	
ν_e	13.8 ± 10.3 (flux) ± 1.4 (exp.) ± 0.3 (stat.)
ν_μ	29.4 ± 8.0 (flux) ± 3.8 (exp.) ± 0.4 (stat.)
Total	**43.5 ± 18.2 (41.9%)**
Data	34
"Other" region	
ν_e	6.3 ± 3.6 (flux) ± 0.8 (exp.) ± 0.19 (stat.)
ν_μ	14.9 ± 2.7 (flux) ± 2.2 (exp.) ± 0.3 (stat.)
Total	**21.3 ± 6.9 (32.2%)**
Data	17

TABLE VIII. Breakdown of the neutrino composition and data yields in the signal region (SR), and in the Preshower, Calorimeter, Magnet, and "Other" regions (excluding events passing signal region selections). Listed are data and neutrino yields as predicted from MC in 57.7 fb^{-1}, also split by neutrino flavour. Uncertainties on the flux, as well as experimental uncertainties further discussed in Section VII, are also given.

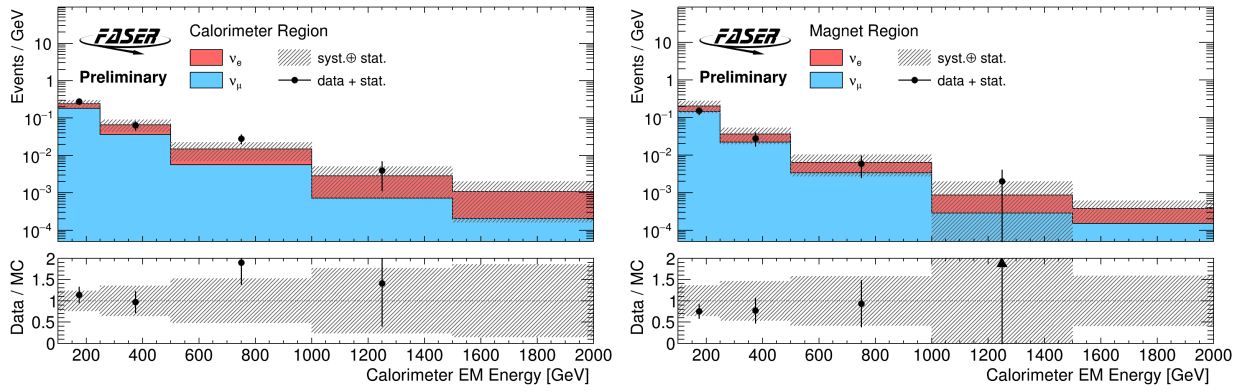

FIG. 12. Calorimeter energy distributions in the calorimeter (left) and magnet (right) regions. The uncertainty band includes MC statistical uncertainties, experimental uncertainties, and uncertainties on the neutrino background flux. The last bin includes the overflow.

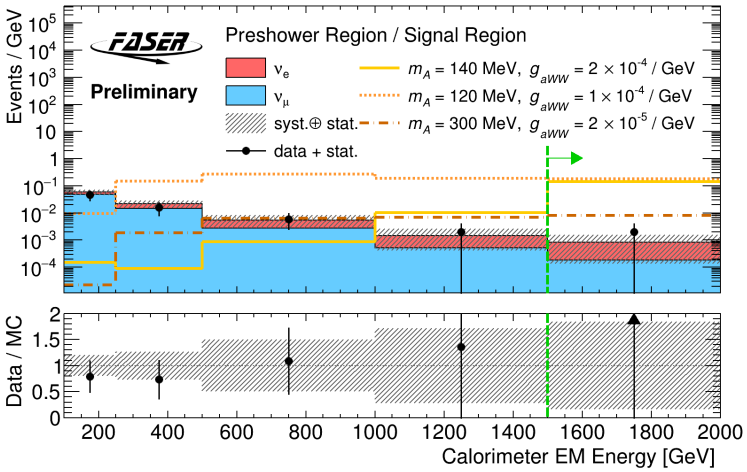

FIG. 13. Calorimeter energy distribution in the preshower and signal region, showing the neutrino background composition, separated according to neutrino flavour. The last bin includes the overflow.

[1] J. L. Feng, I. Galon, F. Kling, and S. Trojanowski, "ForwArd Search ExpeRiment at the LHC," *Phys. Rev. D* **97** (2018) no. 3, 035001, arXiv:1708.09389 [hep-ph].

[2] **FASER** Collaboration, A. Ariga *et al.*, "Letter of Intent for FASER: ForwArd Search ExpeRiment at the LHC," arXiv:1811.10243 [physics.ins-det].

[3] **FASER** Collaboration, A. Ariga *et al.*, "Technical Proposal for FASER: ForwArd Search ExpeRiment at the LHC," arXiv:1812.09139 [physics.ins-det].

[4] **FASER** Collaboration, H. Abreu *et al.*, "The FASER Detector," arXiv:2207.11427 [physics.ins-det].

[5] **FASER** Collaboration, H. Abreu *et al.*, "First Direct Observation of Collider Neutrinos with FASER at the LHC," *Phys. Rev. Lett.* **131** (2023) no. 3, 031801, arXiv:2303.14185 [hep-ex].

[6] **FASER** Collaboration, "Technical Proposal: FASERnu," arXiv:2001.03073 [physics.ins-det].

[7] **FASER** Collaboration, "Observation of High-Energy Electron Neutrino Interactions with FASER's Emulsion Detector at the LHC," tech. rep., CERN, Geneva, 2023. https://cds.cern.ch/record/2868284.

[8] **FASER** Collaboration, "First Measurement of the ν_e and ν_μ Interaction Cross Sections at the LHC with FASER's Emulsion Detector," arXiv:2403.12520 [hep-ex].

[9] **FASER** Collaboration, A. Ariga *et al.*, "FASER's physics reach for long-lived particles," *Phys. Rev. D* **99** (2019) no. 9, 095011, arXiv:1811.12522 [hep-ph].

[10] **FASER** Collaboration, H. Abreu *et al.*, "Search for dark photons with the FASER detector at the LHC," *Phys. Lett. B* **848** (2024) 138378, arXiv:2308.05587 [hep-ex].

[11] R. D. Peccei and H. R. Quinn, "CP Conservation in the Presence of Pseudoparticles," *Phys. Rev. Lett.* **38** (Jun, 1977) 1440–1443.

[12] F. Wilczek, "Problem of Strong P and T Invariance in the Presence of Instantons," *Phys. Rev. Lett.* **40** 279–282.

[13] S. Weinberg, "A New Light Boson?," *Phys. Rev. Lett.* **40** (Jan, 1978) 223–226.

[14] E. Izaguirre, T. Lin, and B. Shuve, "Searching for Axionlike Particles in Flavor-Changing Neutral Current Processes," *Phys. Rev. Lett.* **118** (2017) no. 11, 111802, arXiv:1611.09355 [hep-ph].

[15] S. Gori, G. Perez, and K. Tobioka, "KOTO vs. NA62 Dark Scalar Searches," arXiv:2005.05170 [hep-ph].

[16] F. Kling and S. Trojanowski, "Looking forward to test the KOTO anomaly with FASER," *Phys. Rev. D* **102** (2020) no. 1, 015032, arXiv:2006.10630 [hep-ph].

[17] J. Beacham *et al.*, "Physics Beyond Colliders at CERN: Beyond the Standard Model Working Group Report," *J. Phys. G* **47** (2020) no. 1, 010501, arXiv:1901.09966 [hep-ex].

[18] F. Kling and S. Trojanowski, "Forward Experiment Sensitivity Estimator for the LHC and Future Hadron Colliders," *Phys. Rev. D* **104** (2021) no. 3, 035012, arXiv:2105.07077 [hep-ph].

[19] **LHCb** Collaboration, *LHCb Calorimeters: Technical Design Report*. CERN, Geneva, 2000. http://cds.cern.ch/record/494264.

[20] **FASER** Collaboration, "The Trigger and Data Acquisition System of the FASER Experiment," *JINST* **16** (2021) no. 12, P12028, arXiv:2110.15186 [physics.ins-det].

[21] **ATLAS** Collaboration, "Preliminary Analysis of the Luminosity Calibration of the ATLAS 13.6 TeV Data Recorded in 2022." ATL-DAPR-PUB-2023-001, 2023. https://cds.cern.ch/record/2853525.

[22] G. Avoni *et al.*, "The new LUCID-2 detector for luminosity measurement and monitoring in ATLAS," *JINST* **13** (2018) no. 07, P07017.

[23] **ATLAS** Collaboration, G. Aad *et al.*, "Luminosity determination in pp collisions at $\sqrt{s} = 13$ TeV using the ATLAS detector at the LHC," *Eur. Phys. J. C* **83** (2023) no. 10, 982, arXiv:2212.09379 [hep-ex].

[24] L. Buonocore, F. Kling, L. Rottoli, and J. Sominka, "Predictions for Neutrinos and New Physics from Forward Heavy Hadron Production at the LHC," arXiv:2309.12793 [hep-ph].

[25] P. Nason, "A New method for combining NLO QCD with shower Monte Carlo algorithms," *JHEP* **11** (2004) 040, arXiv:hep-ph/0409146.

[26] S. Frixione, P. Nason, and C. Oleari, "Matching NLO QCD computations with Parton Shower simulations: the POWHEG method," *JHEP* **11** (2007) 070, arXiv:0709.2092 [hep-ph].

[27] S. Alioli, P. Nason, C. Oleari, and E. Re, "A general framework for implementing NLO calculations in shower Monte Carlo programs: the POWHEG BOX," *JHEP* **06** (2010) 043, arXiv:1002.2581 [hep-ph].

[28] V. Bertone, R. Gauld, and J. Rojo, "Neutrino Telescopes as QCD Microscopes," *JHEP* **01** (2019) 217, arXiv:1808.02034 [hep-ph].

[29] R. D. Ball, V. Bertone, M. Bonvini, S. Marzani, J. Rojo, and L. Rottoli, "Parton distributions with small-x resummation: evidence for BFKL dynamics in HERA data," *Eur. Phys. J. C* **78** (2018) no. 4, 321, arXiv:1710.05935 [hep-ph].

[30] C. Bierlich, S. Chakraborty, N. Desai, L. Gellersen, I. Helenius, *et al.*, "A Comprehensive Guide to the Physics and Usage of PYTHIA 8.3," arXiv:2203.11601 [hep-ph].

[31] T. Pierog, I. Karpenko, J. M. Katzy, E. Yatsenko, and K. Werner, "EPOS LHC: Test of collective hadronization with data measured at the CERN Large Hadron Collider," *Phys. Rev. C* **92** (2015) no. 3, 034906, arXiv:1306.0121 [hep-ph].

[32] F. Riehn, R. Engel, A. Fedynitch, T. K. Gaisser, and T. Stanev, "Hadronic interaction model Sibyll 2.3d and extensive air showers," *Phys. Rev. D* **102** (2020) no. 6, 063002, arXiv:1912.03300 [hep-ph].

[33] S. Ostapchenko, "Monte Carlo treatment of hadronic interactions in enhanced Pomeron scheme: I. QGSJET-II model," *Phys. Rev. D* **83** (2011) 014018, arXiv:1010.1869 [hep-ph].

[34] T. Sjöstrand, S. Ask, J. R. Christiansen, R. Corke, N. Desai, P. Ilten, S. Mrenna, S. Prestel, C. O. Rasmussen, and P. Z. Skands, "An introduction to PYTHIA 8.2," *Comput. Phys. Commun.* **191** (2015) 159–177, arXiv:1410.3012 [hep-ph].

[35] M. Fieg, F. Kling, H. Schulz, and T. Sjöstrand, "Tuning Pythia for Forward Physics Experiments," *Phys. Rev. D* **109** (2024) no. 1, 016010, arXiv:2309.08604 [hep-ph].

[36] F. Kling and L. J. Nevay, "Forward Neutrino Fluxes at the LHC," *Phys. Rev. D* **104** (2021) no. 11, 113008, arXiv:2105.08270 [hep-ph].

[37] **FASER** Collaboration, "Neutrino Rate Predictions for FASER," arXiv:2402.13318 [hep-ex].

[38] **GENIE** Collaboration, "Hadronization Model Tuning in GENIE v3," *Phys. Rev. D* **105** (2022) no. 1, 012009, arXiv:2106.05884 [hep-ph].

[39] C. Andreopoulos *et al.*, "The GENIE Neutrino Monte Carlo Generator," *Nucl. Instrum. Meth.* **A614** (2010) 87–104, arXiv:0905.2517 [hep-ph].

[40] C. Andreopoulos, C. Barry, S. Dytman, H. Gallagher, T. Golan, *et al.*, "The GENIE Neutrino Monte Carlo Generator: Physics and User Manual," arXiv:1510.05494 [hep-ph].

[41] A. Bodek and U. K. Yang, "Modeling deep inelastic cross-sections in the few GeV region," *Nucl. Phys. B Proc. Suppl.* **112** (2002) 70–76, arXiv:hep-ex/0203009.

[42] A. Bodek, I. Park, and U.-k. Yang, "Improved low Q**2 model for neutrino and electron nucleon cross sections in few GeV region," *Nucl. Phys. B Proc. Suppl.* **139** (2005) 113–118, arXiv:hep-ph/0411202.

[43] A. Bodek and U. ki Yang, "Axial and Vector Structure Functions for Electron- and Neutrino- Nucleon Scattering Cross Sections at all Q^2 using Effective Leading order Parton Distribution Functions," arXiv:1011.6592 [hep-ph].

[44] A. Candido, A. Garcia, G. Magni, T. Rabemananjara, J. Rojo, and R. Stegeman, "Neutrino Structure Functions from GeV to EeV Energies," *Journal of High Energy Physics* **2023** (May, 2023) .

[45] Y. S. Jeong and M. H. Reno, "Neutrino Cross Sections: Interface of Shallow- and Deep-inelastic Scattering for Collider Neutrinos," arXiv:2307.09241 [hep-ph].

[46] G. Battistoni, T. Boehlen, F. Cerutti, P. W. Chin, L. S. Esposito, *et al.*, "Overview of the FLUKA Code," *Annals of Nuclear Energy* **82** (2015) 10–18.

[47] A. Ferrari, P. R. Sala, A. Fasso, and J. Ranft, *FLUKA: A Multi-particle Transport Code (Program Version 2005)*. CERN Yellow Reports: Monographs. CERN, Geneva, 2005. http://cds.cern.ch/record/898301.

[48] T. T. Böhlen, F. Cerutti, M. P. W. Chin, A. Fasso, A. Ferrari, *et al.*, "The FLUKA Code: Developments and Challenges for High Energy and Medical Applications," *Nucl. Data Sheets* **120** (2014) 211–214.

[49] **GEANT4** Collaboration, S. Agostinelli *et al.*, "GEANT4: A Simulation Toolkit," *Nucl. Instrum. Meth.* **A506** (2003) 250–303.

[50] **FASER** Collaboration, "CALYPSO Software Framework,". https://gitlab.cern.ch/faser/calypso.

[51] **ATLAS** Collaboration, "The ATLAS Collaboration Software and Firmware." ATL-SOFT-PUB-2021-001, 2021. https://cds.cern.ch/record/2767187.

[52] **ATLAS** Collaboration, "ATLAS ATHENA Software,". https://zenodo.org/record/2641997#.XhWRDC2ZPyI.

[53] **FASER** Collaboration, "The FASER W-Si High Precision Preshower Technical Proposal," tech. rep., CERN, Geneva, 2022. https://cds.cern.ch/record/2803084.

[54] M. Baak, G. J. Besjes, D. Côte, A. Koutsman, J. Lorenz, and D. Short, "HistFitter software framework for statistical data analysis," *Eur. Phys. J. C* **75** (2015) 153, arXiv:1410.1280 [hep-ex].

[55] A. L. Read, "Modified Frequentist Analysis of Search Results (The CLs Method),". https://cds.cern.ch/record/451614/files/p81.pdf.

[56] **BaBar** Collaboration, "Search for an Axion-Like Particle in B Meson Decays," arXiv:2111.01800 [hep-ex].

[57] J. Jaeckel, P. C. Malta, and J. Redondo, "Decay photons from the axionlike particles burst of type II supernovae," *Phys. Rev. D* **98** (2018) no. 5, 055032, arXiv:1702.02964 [hep-ph].

[58] J. D. Bjorken, S. Ecklund, W. R. Nelson, A. Abashian, C. Church, *et al.*, "Search for Neutral Metastable Penetrating Particles Produced in the SLAC Beam Dump," *Phys. Rev. D* **38** (Dec, 1988) 3375–3386.

[59] J. Jaeckel and M. Spannowsky, "Probing MeV to 90 GeV axion-like particles with LEP and LHC," *Phys. Lett. B* **753** (2016) 482–487, arXiv:1509.00476 [hep-ph].

[60] **E949** Collaboration, A. V. Artamonov *et al.*, "Search for the decay K+ to pi+ gamma gamma in the pi+ momentum region P > 213 MeV/c," *Phys. Lett. B* **623** (2005) 192–199, arXiv:hep-ex/0505069.

[61] **E949** Collaboration, A. V. Artamonov *et al.*, "Study of the decay $K^+ \to \pi^+ \nu\bar{\nu}$ in the momentum region $140 < P_\pi < 199$ MeV/c," *Phys. Rev. D* **79** (2009) 092004, arXiv:0903.0030 [hep-ex].

[62] **KOTO** Collaboration, J. K. Ahn *et al.*, "Search for the $K_L \to \pi^0 \nu\overline{\nu}$ and $K_L \to \pi^0 X^0$ decays at the J-PARC KOTO experiment," *Phys. Rev. Lett.* **122** (2019) no. 2, 021802, arXiv:1810.09655 [hep-ex].

[63] **KTeV** Collaboration, E. Abouzaid *et al.*, "Final Results from the KTeV Experiment on the Decay $K_L \to \pi^0\gamma\gamma$," *Phys. Rev. D* **77** (2008) 112004, arXiv:0805.0031 [hep-ex].

[64] S. Gori, G. Perez, and K. Tobioka, "KOTO vs. NA62 Dark Scalar Searches," *JHEP* **08** (2020) 110, arXiv:2005.05170 [hep-ph].

[65] **NA62** Collaboration, C. Lazzeroni *et al.*, "Study of the $K^\pm \to \pi^\pm\gamma\gamma$ decay by the NA62 experiment," *Phys. Lett. B* **732** (2014) 65–74, arXiv:1402.4334 [hep-ex].

[66] M. Bauer, M. Neubert, and A. Thamm, "Collider Probes of Axion-Like Particles," *JHEP* **12** (2017) 044, arXiv:1708.00443 [hep-ph].